BC RESEARCH ARTICLE



Probing the role of protein conformational changes in the mechanism of prenylated-FMN-dependent phenazine-1-carboxylic acid decarboxylase

Received for publication, August 21, 2023, and in revised form, November 30, 2023 Published, Papers in Press, January 3, 2024, https://doi.org/10.1016/j.jbc.2023.105621

Prathamesh M. Datar¹, Soumil Y. Joshi², Sanket A. Deshmukh², and E. Neil G. Marsh^{1,3,*}

From the ¹Department of Chemistry, University of Michigan, Ann Arbor, Michigan, USA; ²Department of Chemical Engineering, Virginia Polytechnic Institute and State University, Blacksburg, Virginia, USA; ³Department of Biological Chemistry, University of Michigan, Ann Arbor, Michigan, USA

Reviewed by members of the JBC Editorial Board. Edited by Chris Whitfield

Phenazine-1-carboxylic acid decarboxylase (PhdA) is a prenylated-FMN-dependent (prFMN) enzyme belonging to the UbiD family of decarboxylases. Many UbiD-like enzymes catalyze (de)carboxylation reactions on aromatic rings and conjugated double bonds and are potentially valuable industrial catalysts. We have investigated the mechanism of PhdA using a slow turnover substrate, 2,3-dimethylquinoxaline-5carboxylic acid (DQCA). Detailed analysis of the pH dependence and solvent deuterium isotope effects associated with the reaction uncovered unusual kinetic behavior. At low substrate concentrations, a substantial *inverse* solvent isotope effect (SIE) is observed on V_{max}/K_M of ~ 0.5 when reaction rates of DQCA in H2O and D2O are compared. Under the same conditions, a normal SIE of 4.15 is measured by internal competition for proton transfer to the product. These apparently contradictory results indicate that the SIE values report on different steps in the mechanism. A proton inventory analysis of the reaction under V_{max}/K_M and V_{max} conditions points to a "medium effect" as the source of the inverse SIE. Molecular dynamics simulations of the effect of D₂O on PhdA structure support that D₂O reduces the conformational lability of the enzyme and results in a more compact structure, akin to the active, "closed" conformer observed in crystal structures of some UbiD-like enzymes. Consistent with the simulations, PhdA was found to be more stable in D₂O and to bind DQCA more tightly, leading to the observed rate enhancement under V_{max}/K_M conditions.

Prenylated flavin mononucleotide (prFMN) is the cofactor for a recently discovered class of (de)carboxylase enzymes that remove or attach carboxylate groups at sp²-hybridized carbon atoms (1, 2). prFMN-dependent enzymes are also referred to as "UbiD-like" enzymes, based on a prFMNdependent decarboxylase involved in bacterial ubiquinone biosynthesis (3). Although, so far, few of these enzymes have been characterized in detail, the UbiD family of decarboxylases are widely distributed among microbes where many

In prFMN, the isoalloxazine moiety of the flavin is modified by the addition of an isoprene-derived 6-membered ring that spans N5 and C6 of the flavin (Fig. 1). This modification occurs on reduced FMN and is catalyzed by a specialized prenyl transferase, with either dimethylallyl phosphate or dimethylallyl pyrophosphate as the prenyl donor. Upon reoxidization, prFMN forms a nitrogen ylide, and it is this unusual modification that converts this ubiquitous redox cofactor into one that facilitates (de)carboxylation reactions at sp²-hybridized carbon atoms (6-9).

The mechanism by which prFMN-dependent enzymes catalyze decarboxylation reactions hinges upon the reactivity of the nitrogen ylide towards electron-rich unsaturated C-C double bonds. For ferulic acid decarboxylase (FDC), which is the best-understood enzyme, experimental evidence (2, 10-15)points to the reaction being initiated through a 1,3-dipolar cycloaddition between the nitrogen ylide with the double bond adjacent to the carboxyl group of the substrate (akin to $E.I_1$ in Fig. 1) (11, 13). This allows the flavin nucleus to act as an electron sink in the subsequent decarboxylation step (2). However, for enzymes such as AroY(16) that decarboxylate electron-rich aromatic carboxylic acids, the mechanism is more likely to involve electrophilic addition of the substrate to prFMN (16).

Recently, a novel prFMN-dependent enzyme, PhdA, was discovered which catalyzes the decarboxylation of the redoxactive metabolite phenazine-1-carboxylic acid (PCA) to phenazine (17). Phenazines are secreted by a wide variety of bacteria and are integral to biofilm formation and anoxic survival (18). Biofilm formation in a clinical setting poses a serious health risk because the biofilm renders pathogens such as Pseudomonas aeruginosa resistant to antibiotic treatment (19). In contrast, in an agricultural setting, phenazines secreted by Pseudomonas spp. are beneficial as they protect cereal crops from various parasitic and fungal diseases (20).

^{*} For correspondence: E. Neil G. Marsh, nmarsh@umich.edu.



appear to be involved in the metabolism of aromatic compounds. Because of their potential to catalyze (de)carboxylation reactions at otherwise unreactive carbon centers, UbiDlike enzymes have attracted interest as selective and environmentally benign catalysts for organic synthesis (4-6).

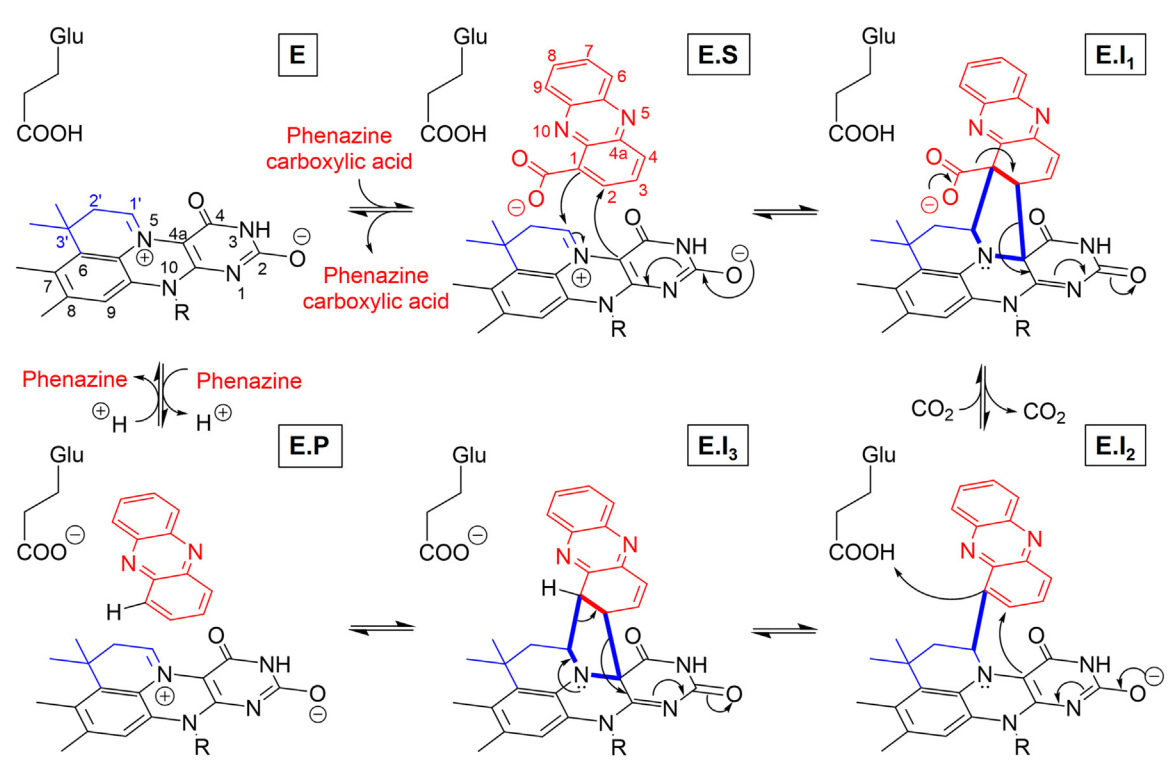


Figure 1. Proposed dipolar cycloaddition reaction mechanism for PhdA-catalyzed decarboxylation of PCA. E, free enzyme; E.S, Michaelis complex; E.I₁, E.I₂ and E.I₃, covalent intermediates; E.P., Enzyme-product complex.

In our previous work, we established conditions for reconstituting PhdA with prFMN and surveyed its substrate scope. We established that the enzyme decarboxylates the oxidized form of phenazine, which earlier studies had left open to question. We showed that, in addition to PCA, PhdA will catalyze the decarboxylation of a wide range of aromatic compounds including such unreactive compounds as anthracene-1-carboxylic acid, albeit at slow rates. We also showed that PhdA catalyzes the exchange of deuterium into phenazine and measured the kinetics of this reaction. Our kinetic analysis suggested that deprotonation of phenazine would likely be the rate-determining step for the reverse carboxylation reaction. Based on these results, we proposed a 1,3-dipolar cycloaddition mechanism for PhdA, akin to the reaction catalyzed by FDC (Fig. 1) (21).

Here we have analyzed the kinetics of the PhdA-catalyzed decarboxylation in more detail. We have compared the reaction of the physiological substrate, PCA, with the slow substrate 2,3-dimethylquinoxaline-5-carboxylic acid (DQCA). The kinetics of both substrates display an unusual dependence on D_2O , with the observed isotope effects being more prominent for DQCA. When comparing the ratio of proteated to deuterated products formed for a reaction conducted in H_2O/D_2O mixtures, the enzyme discriminates against the transfer of the heavy isotope, resulting in a *normal* SIE. However, when the rate of the reaction is measured under V_{max}/K_M conditions in either 100% H_2O or 98% D_2O , the reaction exhibits an *inverse* SIE. Our studies suggest that the unusual *inverse* SIE can be explained by a medium effect related to protein

conformational changes. We investigated the nature of this conformation change by performing all-atom molecular dynamics (MD) simulations using the crystal structure of PhdA (PDB ID: 7PDA) (22) as a starting point. We also developed a kinetic model of the reaction that accounts for these apparently contradictory isotope effects.

Results

A note on nomenclature

The solvent deuterium isotope effects described here were measured by two different methods which we distinguish using the following nomenclature: To denote isotope effects measured by direct comparison of reaction velocities in H₂O and D_2O_2 , we use the nomenclature of Quinn (1991) (23). Thus, ^{D2O}V denotes the solvent isotope effect on V_{max} calculated as the ratio of the reaction velocities in H2O and D₂O measured at saturating substrate concentrations. Similarly, $^{D2O}V/K$ denotes the solvent isotope effect on V_{max}/K_M , calculated as the ratio of the reaction rates in H2O and D2O measured under low substrate concentrations ([S]<< K_M). We use the term "product isotope effect", PIE (24), to denote an isotope effect involving an enzyme-mediated transfer of a solvent proton to a non-exchangeable site in the product (E.I₂ to E.I3, Fig. 1). PIE values are measured by performing the reaction in H₂O/D₂O mixtures and comparing the distribution of proteated to deuterated products (14, 25). As such, PIE is a V_{max}/K_M isotope effect associated with the exchange of solvent protons with the enzyme.

Solvent isotope effects for PhdA reacting with PCA

Decarboxylation reactions catalyzed by UbiD-like enzymes involve the transfer of a solvent proton to carbon, often mediated by an active-site glutamate residue (Fig. 1E.I₂ to $E.I_3$), that is subject to an isotope effect (14). Therefore, we reasoned that investigating the kinetic behavior of PhdA in buffered D₂O might be mechanistically informative. Solvent deuterium content affects the pKa values of most acids including enzymatic functional groups (24), which necessitates measuring isotope effects in a pL-independent region (L = H or D) of the pL-rate profile. Furthermore, comparing isotope effects under V_{max} (high substrate) and V_{max}/K_M (low substrate) provides information about different regions of the kinetic mechanism. Previously, we determined $k_{cat} = 155 \pm$ 4 min^{-1} and $K_M = 53 \pm 2 \mu\text{M}$ for the PhdA-catalyzed decarboxylation of PCA (21). Based on these parameters, we measured pL-rate profiles under V_{max} ([PCA] = 500 μ M; $\sim 10 \text{ x } K_M$) or V_{max}/K_M ([PCA] = 15 μ M; $\sim K_M/3$) conditions (Fig. 2).

Under both conditions, the reaction exhibited a classical bell-shaped activity profile. For V_{max}/K_M conditions in H₂O, the apparent pK_a values for the acidic (pK_{a1}) and basic (pK_{a2}) limbs are 6.7 ± 0.3 and 7.0 ± 0.3 , respectively. The values under V_{max} conditions are shifted further apart: pK_{a1} = 6.2 ± 0.2 and $pK_{a2} = 7.6 \pm 0.2$. The apparent pK_a values measured under V_{max} and V_{max}/K_M conditions reflect those of the enzymesubstrate complex and free enzyme respectively. The pKa of the N1 proton (refer to Fig. 1 for atom numbering) in reduced FMN is \sim 6.2 to 6.9, based on the local environment (26). Therefore, we hypothesize that pK_{a1} of PhdA's pH-rate profile reflects the N1 proton on prFMN, which needs to be deprotonated for activity. On the other hand, pKa2 most likely reflects the active site glutamate (Glu269 in PhdA), which needs to be protonated. Repeating the measurements in D₂O resulted in a small but significant upward shift of ~0.3 pH units to the pKa values.

Having established the pL profile for PhdA reacting with PCA under V_{max} and V_{max}/K_M conditions, we measured the corresponding SIE values, ^{D2O}V and $^{D2O}V/K$, by direct comparison of the rates of reaction at the pL maxima for each condition. These measurements yielded $^{D2O}V = 0.93 \pm 0.12$ (n = 6) and $^{D2O}V/K = 0.75 \pm 0.17$ (n = 6). Similar to previous studies with FDC (14), D2OV for PhdA is unity within error, implying that proton transfer is not rate-limiting under V_{max} conditions. However, it is surprising that D2OV/K appears slightly inverse. Apparent inverse SIE observed in some enzymes, for example, NAD-Malic enzyme (27), has been attributed to the increased viscosity of D2O. However, when we measured the values of V_{max} and V_{max}/K_M under increasing concentrations of viscosogens such as sucrose or glucose (Fig. S1), the rates of reaction were either slightly decreased or unaffected by the presence of the viscosogen. These observations indicate that viscosity differences are not responsible for the apparent *inverse* SIE.

To gain further insight into the mechanism, we measured the product isotope effect (PIE) for the transfer of solvent

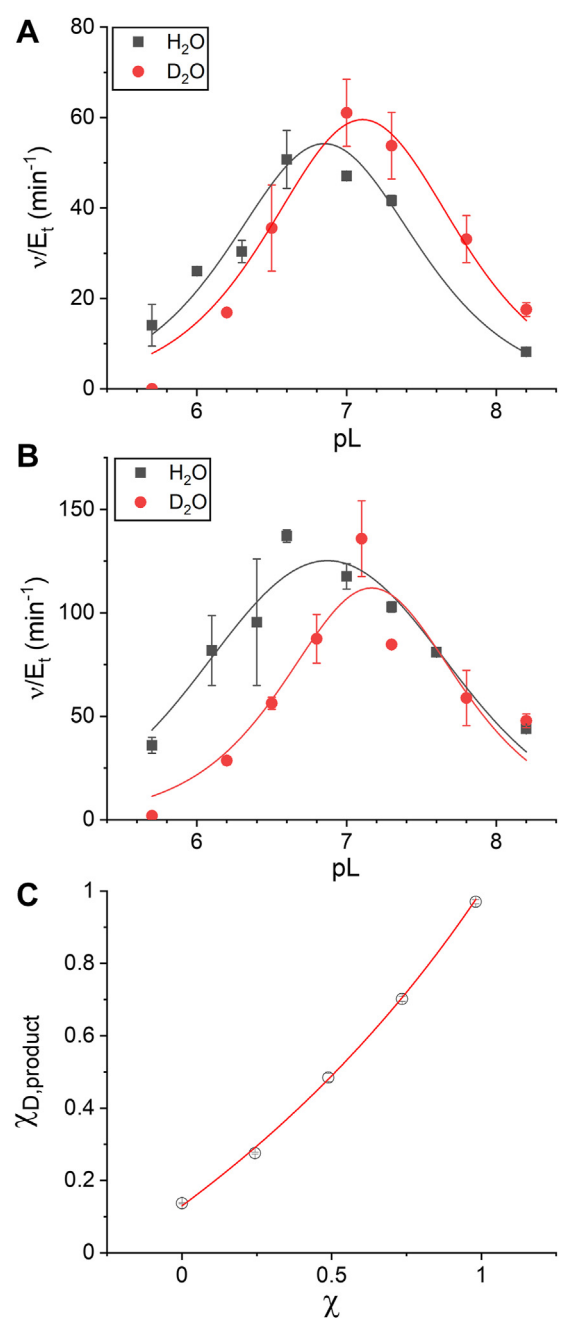


Figure 2. pH and pD rate profiles of the decarboxylation of PCA by **PhdA**. A, for the reaction monitored at low [PCA] $(K_M/3, V_{max}/K_M \text{ conditions})$. B, for the reaction monitored at high [PCA] (10 x K_M , V_{max} conditions). The reaction rate normalized by the enzyme concentration (v/E_t) is plotted as a function of pL (pH or pD). Data are fitted assuming 2 ionizable groups contribute to the rate profile. C, determining PIE for the transfer of deuterium on route to phenazine. The mole fraction of deuterated phenazine $(\chi_{D.product})$ is plotted as a function of solvent D-atom fraction (χ) and the isotope effect is calculated by fitting the data to Equation 1. Each data point is an average of two replicates and error bars represent the standard error of the mean.

deuterium to phenazine in H_2O/D_2O mixtures (Fig. 2C). PhdA-catalyzed decarboxylation of PCA was monitored at pL = 7 in buffers containing increasing D-atom fraction (χ), and the phenazine produced was analyzed by LC-MS to determine the mole fraction of deuterium appearing in the product, $\chi_{D,product}$. PIE was calculated from these data by fitting



them to Equation 1 (Refer to Supporting information for derivation):

$$\chi_{D.product} = \frac{B + \left(\frac{1}{PIE} - B\right)\chi}{\left(\frac{1}{PIE} - 1\right)\chi + 1}$$
(1)

Here, B is the natural 13 C isotopic abundance in the product and corrects for the non-zero value of $\chi_{D,product}$ at $\chi=0$ (refer to SI for further explanation). The SIE on V_{max}/K_M calculated from product distribution ($PIE=1.43\pm0.06$) is small and, as expected, *normal*. This is in contrast to the value calculated by the direct comparison of reaction rates ($^{D2O}V/K=0.75\pm0.17$). The difference in the SIE values suggests that the two effects arise from different steps in the mechanism.

Solvent isotope effects for PhdA reacting with DQCA

The reactions of enzymes with "slow" substrates can often be mechanistically informative because they may uncover steps that are kinetically masked in reactions with the physiological substrates. Previously, we identified 2,3-dimethylquinoxaline-5-carboxylic acid (DQCA) as a substrate for PhdA (21); therefore, we reasoned that a detailed examination of the kinetics of DQCA decarboxylation might be informative. We first determined k_{cat} and K_M for DQCA reacting with PhdA at pH 7.0 and 22 °C (Fig. S2). The k_{cat} = 6.1 ± 0.1 min⁻¹ is approximately 25-fold slower than that for PCA, whereas K_M = 509 ± 42 μ M is \sim 10-fold higher than that for PCA. The catalytic efficiency (k_{cat}/K_M) for DQCA is therefore \sim 250-fold lower than for PCA.

We then examined the pL-rate profile for DQCA reacting with PhdA in more detail (Fig. 3). Unsurprisingly, in H₂O, the bell-shaped pH profile is similar to that observed for the reaction of PCA. Under V_{max} conditions ([DQCA] = 10 mM; $\sim 20 \times K_{\rm M}$), pK_{a1} = 6.2 ± 0.1 and pK_{a2} = 7.7 ± 0.1, whereas under V_{max}/K_M conditions ([DQCA] = 30 μ M; $K_M/16$), pK_{a1} = 6.7 ± 0.3 and pK_{a2} = 7.1 ± 0.4 respectively. We then repeated the measurements in D₂O and determined the apparent pK_a values as pK_{a1} = 6.4 ± 0.1, pK_{a2} = 8.0 ± 0.1 under V_{max} conditions and pK_{a1} = 6.9 \pm 0.4, pK_{a2} = 7.4 \pm 0.4 under V_{max}/K_{M} conditions. Like PCA, the pKa values are shifted ~0.3 units higher in D_2O . Under V_{max}/K_M conditions a substantial inverse SIE is evident, although under V_{max} conditions the solvent isotope effect is close to unity. We measured $^{D2O}V/K$ $(0.53 \pm 0.01, n = 6)$ and $^{D2O}V(0.9 \pm 0.04, n = 5)$ at pL = 7. We also measured the values at the respective pL maxima and observed no significant differences ($^{D2O}V/K \sim 0.5$ –0.6 for both measurements). Therefore, for simplicity, all future isotope effect studies were performed at pL = 7. To verify that the inverse isotope effects did not arise from changes in viscosity, we examined the PhdA-catalyzed decarboxylation of DQCA in the presence of sucrose and glucose as viscosogens (Fig. S3). Although the reaction rate increased slightly (~10%) with increasing viscosogen concentration, it cannot explain the significantly higher reaction rate in D2O.

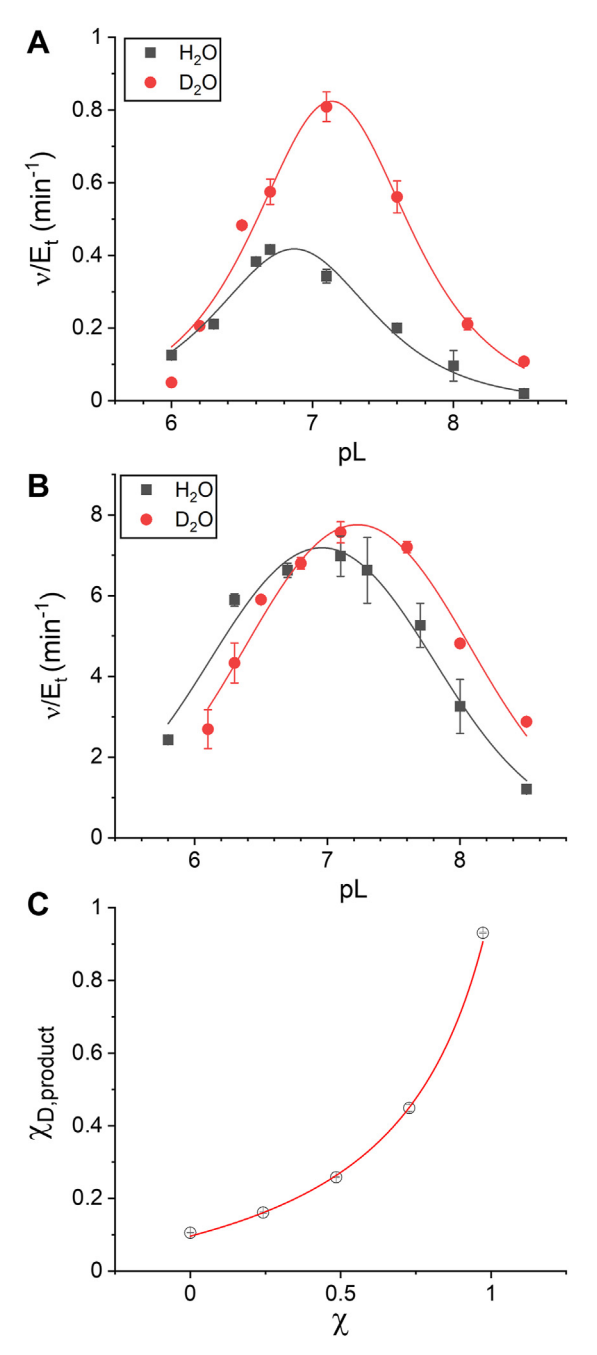


Figure 3. pH and pD rate profiles of the decarboxylation of DQCA by PhdA. A, for the reaction monitored at low [DQCA] ($K_M/16$; V_{max}/K_M conditions). B, for the reaction monitored at high [DQCA] ($20 \times K_{Mi}$; V_{max} conditions). The reaction rate, normalized with respect to the enzyme concentration, (V/E_v) is plotted as a function of pL (pH or pD). Data are fitted assuming 2 ionizable groups contribute to the rate profile. C, determining PIE for the transfer of deuterium on route to 2,3-dimethylquinoxaline (DQ). The mole fraction of deuterated DQ ($\chi_{D,product}$) is plotted as a function of solvent D-atom fraction (χ) and the isotope effect is calculated by fitting the data to Equation 1. Each data point is an average of two replicates and error bars represent the standard error of the mean.

We also measured *PIE* for the transfer of deuterium into 2,3-dimethylquinoxaline (DQ), the product derived from DQCA, using a similar methodology and analysis as described above for PCA (Fig. 3C). In this case, the SIE is much larger and *normal* ($PIE = 4.15 \pm 0.22$). This value is quite typical for the transfer of a deuteron from a solvent-exchangeable residue to carbon (28).



In summary, the D2OV, D2OV/K, and PIE values measured for the decarboxylation of DQCA follow a similar trend to those observed for PCA, but with the corresponding SIE values becoming more pronounced. It appears that, because DQCA is a poor surrogate substrate for PhdA, the isotopically sensitive steps in the mechanism become more rate limiting when compared to the physiological substrate, PCA.

Proton inventory analysis

The seemingly contradictory values of D2OV/K and PIE suggest the presence of more than one isotopically sensitive step. While the normal PIE is most likely associated with proton transfer from E.I2 to E.I3 (Fig. 1), the source of the *inverse* D2OV/K is less clear. We therefore conducted a proton inventory analysis for the decarboxylation of DQCA, for which the isotope effects are larger. This technique can provide information on the number of exchangeable protons (or deuterons) that actively participate in a reaction (Fig. 4) (23).

For V_{max}/K_M conditions, the rate increases gradually with increasing D-atom fraction (Fig. 4A). The data were fitted to the three simplest mechanisms: one transition state proton in flight (linear proton inventory, Equation 2); one reactant state proton (hyperbolic proton inventory, Equation 3), and a medium effect (exponential proton inventory, Equation 4) (28).

$$v_{\chi} / v_0 = 1 - \chi + \chi \cdot \phi_T \tag{2}$$

$$v_{\chi} / v_0 = \frac{1}{1 - \chi + \chi \cdot \phi_R} \tag{3}$$

$$v_{\rm y} / v_0 = Z^{\chi} \tag{4}$$

where ϕ_T is the fractionation factor of the proton involved in the transition state, ϕ_R is the fractionation factor for a reactant state proton and Z is the value of the overall medium effect in D₂O (here, Z comprises many protic sites, each with an φ value close to unity) (28). Although the data are plausibly fitted by a simple linear function (Equation 2), for the isotope effect to arise from a single transition state proton its fractionation factor would need to be extremely high ($\phi_T = 1.92$). Such a high value for ϕ_T is unprecedented (23). A hyperbolic proton inventory (Equation 3) is attributed to the deprotonation of a reactant state proton with $\phi_R < 1$. While the ϕ_R displayed by Cys residues ($\phi_R \sim 0.55$) (23) is comparable to the observed value of $^{D2O}V/K$, Cys residues are not implicated in the mechanisms of UbiD-like enzymes. Moreover, the crystal structure of PhdA (PDB:7PDA) shows no active site Cys residues that may participate in the reaction. Statistically too, a hyperbolic function fits the data least well.

The midpoint isotope effect (24) is a useful tool to identify the best fit for proton inventory data. It involves calculating the expected values of v_x/v_0 at $\chi = 0.5$ for different fits and comparing them to the experimental value. The expected midpoint isotope effect for a hyperbolic proton inventory in our case is 1.31 ± 0.02 , whereas the experimentally determined value is 1.42 ± 0.04 (n = 6). The *inverse* SIE is therefore unlikely to arise from a single reactant state proton. This leaves a medium effect (Equation 4) as the most plausible interpretation of the data, that is, the SIE arises from a combination of many protic sites with small fractionation factors involved in overall solvent reorganization or conformational change.

Under V_{max} conditions, a dome-shaped proton inventory is obtained (Fig. 4B) which is diagnostic of competing normal and *inverse* isotope effects contributing to ^{D2O}V (29–31). The data may be fitted to Equation 5 which describes this situation (see SI for derivation):

$$v_{\chi} / v_0 = \frac{Z^{\chi}(1 - \chi + \chi.\phi_T)}{1 - \chi + \chi.\psi_T + \chi.\phi_T - \chi.\psi_T.\phi_T}$$
 (5)

Here, Z is the value of the general medium effect in D_2O , ϕ_T is the transition state fractionation factor for the proton transfer and w_7 is its fractional contribution to V_{max} . Equation 5 contains mutual dependency between parameters and therefore satisfactory fits cannot be obtained without "fixing" a parameter. From the value of *PIE*, the upper limit of ϕ_T is 0.24 (refer to SI for further explanation). This can be used to estimate $Z \sim 1.4$ and $w_7 \sim 0.1$. Thus, $D_{2O}V$ arises from a general medium effect (Z) offset by a single transition state proton (ϕ_T) contributing $\sim 10\%$ to the overall rate limitation.

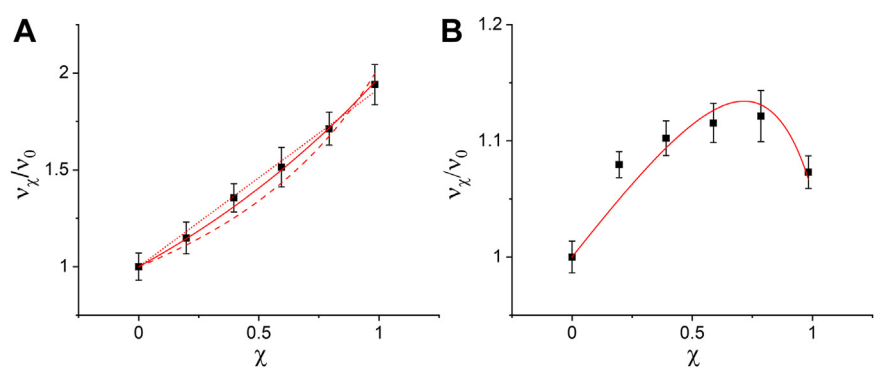


Figure 4. Proton inventory analysis of PhdA catalyzed decarboxylation of DQCA. The reaction velocity (v_χ) relative to 100% H_2O $(\chi = 0)$ plotted as a function of solvent D-atom fraction (χ) under (A) low [DQCA] (V_{max}/K_M conditions) and (B) high [DQCA] (V_{max} conditions). The data in (A) are fitted to Equation 2 (top, —), Equation 3 (bottom, - - -) and Equation 4 (middle, ••••) whereas the data in (B) are fitted to Equation 5 described in the main text. Each data point is an average of two replicates and error bars represent the standard error of the mean.

Origin of the medium effect in PhdA

It is well documented that D_2O alters the stability of proteins, which leads many proteins to unfold more slowly and at higher denaturant concentrations in D_2O (32–35). To examine if PhdA is more stable in D_2O , we compared the urea-induced unfolding of PhdA in buffered H_2O and D_2O by following the red shift in intrinsic protein fluorescence (Fig. S4). The normalized unfolding curves were plotted as a function of urea concentration (Fig. 5*A*). We observe that PhdA unfolds at higher urea concentrations in D_2O than in H_2O . Fitting the curves to a simple two-state model of protein unfolding (see Experimental procedures) gave $K_{1/2}$ for unfolding in $H_2O = 1.54 \pm 0.03$ M and $\Delta G_U = 18 \pm 4$ kJ mol⁻¹ whereas in D_2O , $K_{1/2} = 2.27 \pm 0.04$ M and $\Delta G_U = 23 \pm 6$ kJ mol⁻¹. The higher values for $K_{1/2}$ and ΔG_U indicate that PhdA appears to be more stable in D_2O compared to H_2O .

Conformational stability affects reaction kinetics

With evidence that D_2O affects the stability of the free enzyme, we sought to identify how this effect can manifest in $^{D2O}V/K$. V_{max}/K_M conditions provide information on all the steps from free enzyme up to and including the first irreversible step (Fig. 9) (36). Thus, we hypothesized that this stable conformer in D_2O might favor the formation of the Michaelis complex and subsequent steps in the reaction, leading to an *inverse* $^{D2O}V/K$. To verify this, we first measured the K_M of PCA and DQCA in H_2O and D_2O at pL = 7 (Fig. S2). We observed in both cases that while k_{cat} does not change significantly, the K_M is appreciably lower in D_2O (PCA: $K_M = 49.9 \pm 0.7 \,\mu\text{M}$ in H_2O and $28.6 \pm 1.7 \,\mu\text{M}$ in D_2O ; DQCA: $K_M = 509 \pm 42 \,\mu\text{M}$ in H_2O and $252 \pm 6 \,\mu\text{M}$ in D_2O). The lower K_M value suggests that D_2O favors the capture of substrate to form an effective complex that is poised for turnover (37).

Although changes in K_M are often used as a proxy for K_d , it is well known that this makes assumptions about the rate constants downstream of the E.S complex. We therefore exploited the fact that the slow substrate, DQCA, acts as a competitive inhibitor of the physiological substrate, PCA ([PCA] = 50 μ M), to measure apparent inhibition constants (K_I^{app}) for DQCA in H₂O and D₂O (Fig. 5B). The change in

inhibition is quite striking. In D₂O, DQCA behaves as a much more potent inhibitor, $K_I^{app} = 250 \pm 30 \, \mu\text{M}$, than in H₂O, $K_I^{app} = 2100 \pm 300 \, \mu\text{M}$. The drastically lower K_I^{app} indicates that the decrease in K_M in D₂O could be related to the formation of a more productive Michaelis complex poised appropriately for subsequent steps.

Molecular dynamics simulations show conformational differences in the two solvents

To understand the microscopic origins of the conformational stability exhibited by PhdA in the two solvents, we performed all-atom MD simulations using its crystal structure (PDB:7PDA), over a period of 1 μ s in the presence of explicit H₂O or D₂O molecules. In common with other UbiD-like enzymes, the tertiary structure of PhdA comprises an N-terminal prFMN binding domain, a central α -helix, an oligomerization domain and a C-terminal α -helix (38). Although PhdA is hexameric, the simulations were performed using a monomer, a simplification that greatly expedited the calculations, but was not expected to affect the behavior of active site residues that are located away from the protein-protein interfaces (Fig. S5) (39, 40).

Analysis of the root mean squared deviation (RMSD) of the protein backbone from the starting structure showed a higher value for the protein in H₂O than in D₂O during the initial equilibration period (Fig. 6A). The RMSD was stable for the remainder of the trajectories, except for the data at \sim 750 ns, at which time, larger RMSD values were observed. This perturbation arises from the movement of the C-terminal helix which can be observed in Movies S1 and S2. However, this is likely an artifact because in the quaternary structures of UbiD-like enzymes, the C-terminal helix normally makes extensive contact with other protein subunits (38). Excluding the C-terminal helix from the RMSD analysis removed the discontinuity (Fig. S6). The residue-wise root mean squared fluctuation (RMSF) was calculated for the final 500 ns of the MD trajectories. Consistent with the RMSD analysis, residues in the H2O-solvated system showed greater fluctuations than those in D₂O, even after excluding the C-terminal helix (Fig. 6B). These data indicate that PhdA

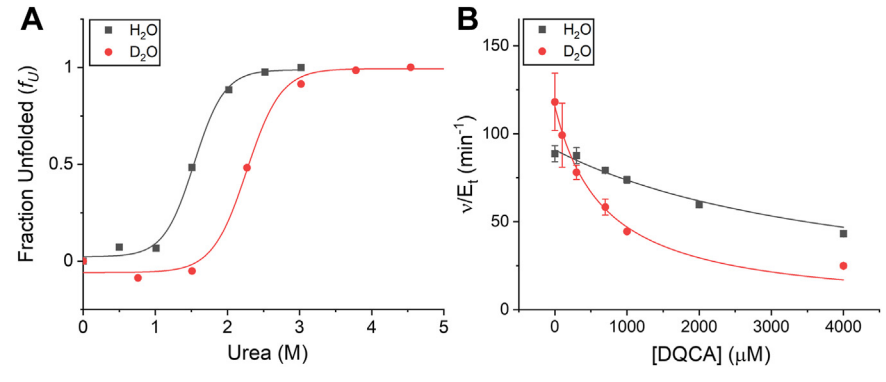


Figure 5. Effect of D_2O on protein stability and substrate binding. A, urea-induced unfolding of PhdA in H_2O and D_2O monitored by red-shift in fluorescence emission spectra. The fraction of unfolded protein is plotted as a function of urea concentration. B, competitive inhibition of PCA decarboxylation by the slower-turnover substrate DQCA in buffered H_2O and D_2O . The residual rate of PCA decarboxylation normalized to enzyme concentration (v/E_1) is plotted as a function of [DQCA]. Each data point is an average of two replicates and error bars represent the standard error of the mean.

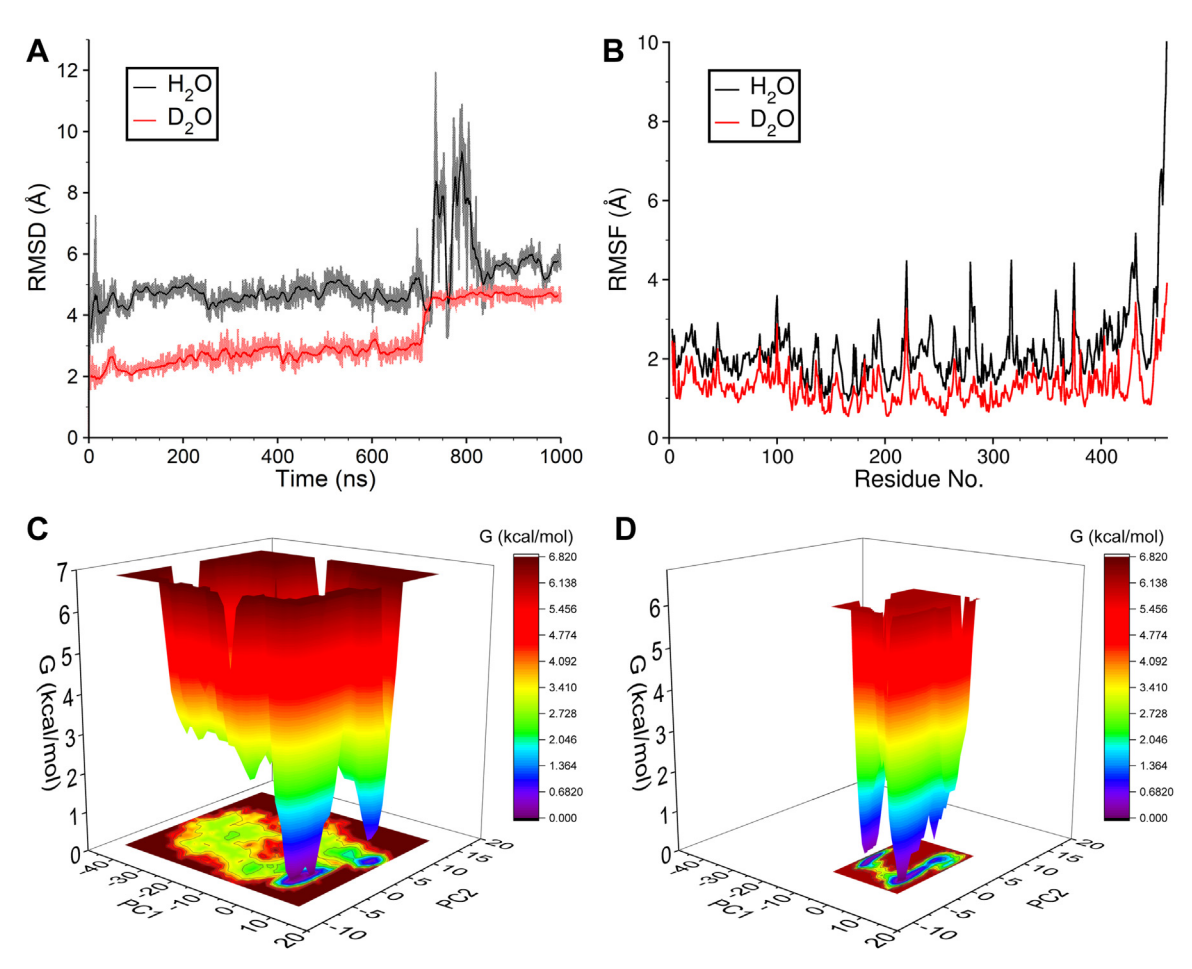


Figure 6. MD simulations of PhdA in H₂O and D₂O. A, RMSD for the protein backbone throughout the simulation run. B, RMSF for protein residues. Free energy landscapes for PhdA monomer in (C) H₂O and (D) D₂O. Colorbar includes the energy values. The x and y axes represent two principal components (PCs) of the proteins with the highest variations. PCs are extracted using a multivariate statistical technique called Principal Component Analysis and represent maximum protein dynamics in lower dimensions. For (A), translucent background lines display data points from the entire simulation trajectory (1,000,000 points) while the solid foreground lines display smoother running averages considering every 2000 points. Analysis in (B) was carried out for the last 500 ns of the simulation trajectories.

is less conformationally mobile when solvated in D2O, compared to H_2O (41).

For validation, protein free-energy landscapes (FELs), which provide a statistical description of the various possible states explored by a protein in MD simulations, were obtained through the Boltzmann inversion of the joint probability density function of the principle components (PCs) (42). The protein in H2O (Fig. 6C) displayed a significantly higher exploration of the conformational space as compared to the protein in D_2O (Fig. 6D). In agreement with our experimental results, the D₂O-solvated protein FEL exhibited prominent narrow troughs indicating highly stable conformations that dominated throughout the simulations, as opposed to broader troughs and multiple conformers separated by low energy barriers in the H₂O-solvated system (Fig. S7). Consistent with this analysis, 80 unique protein conformers were identified for the H_2O -solvated protein whereas only 7 were found in D_2O . These conformers were recognized by calculating the RMSDs between all structures throughout the trajectory and segregating them based on an RMSD cutoff of 2 Å (43).

Overlaying the dominant conformers identified in H₂O and D₂O established significant differences between the two, with an RMSD of 3.82 Å (Fig. S8). Based on their crystal structures, UbiD-like enzymes are known to exhibit distinct 'open' and 'closed' conformers. The distance between the centers-ofmasses (COM) of residues R159 and I416 (residues that are broadly conserved in UbiD-like enzymes) serves as a convenient metric to measure the openness of the active site (44). In the crystal structure of PhdA, solved without substrate-bound, the R–I distance is \sim 14.3 Å, corresponding to an 'open' conformer. However, for the dominant conformers identified in this study, the R–I distance in H_2O increased to ~ 15.7 Å, whereas in D_2O it decreased to ~ 11.2 Å. When calculated over the entire simulation trajectory, the R-I distance in H₂O progressively increased from \sim 14.3 Å to \sim 17.8 Å (Fig. 7A) suggesting significant further domain opening. In contrast, in D_2O , this distance is reduced to $\sim 11.5 \text{ Å}$ (Fig. 7B) indicating its evolution to a more "closed" conformer (Fig. 7C).

Moreover, the RMSF data coupled with a visual inspection of the simulation showed that the active site loop, comprising residues 264 to 279, that contains the catalytic residue E269 was more structured and compact in D_2O . In line with this observation, the distance between the centers of masses of the cofactor and E269 is shorter in D₂O than in H₂O (Fig. 7D).



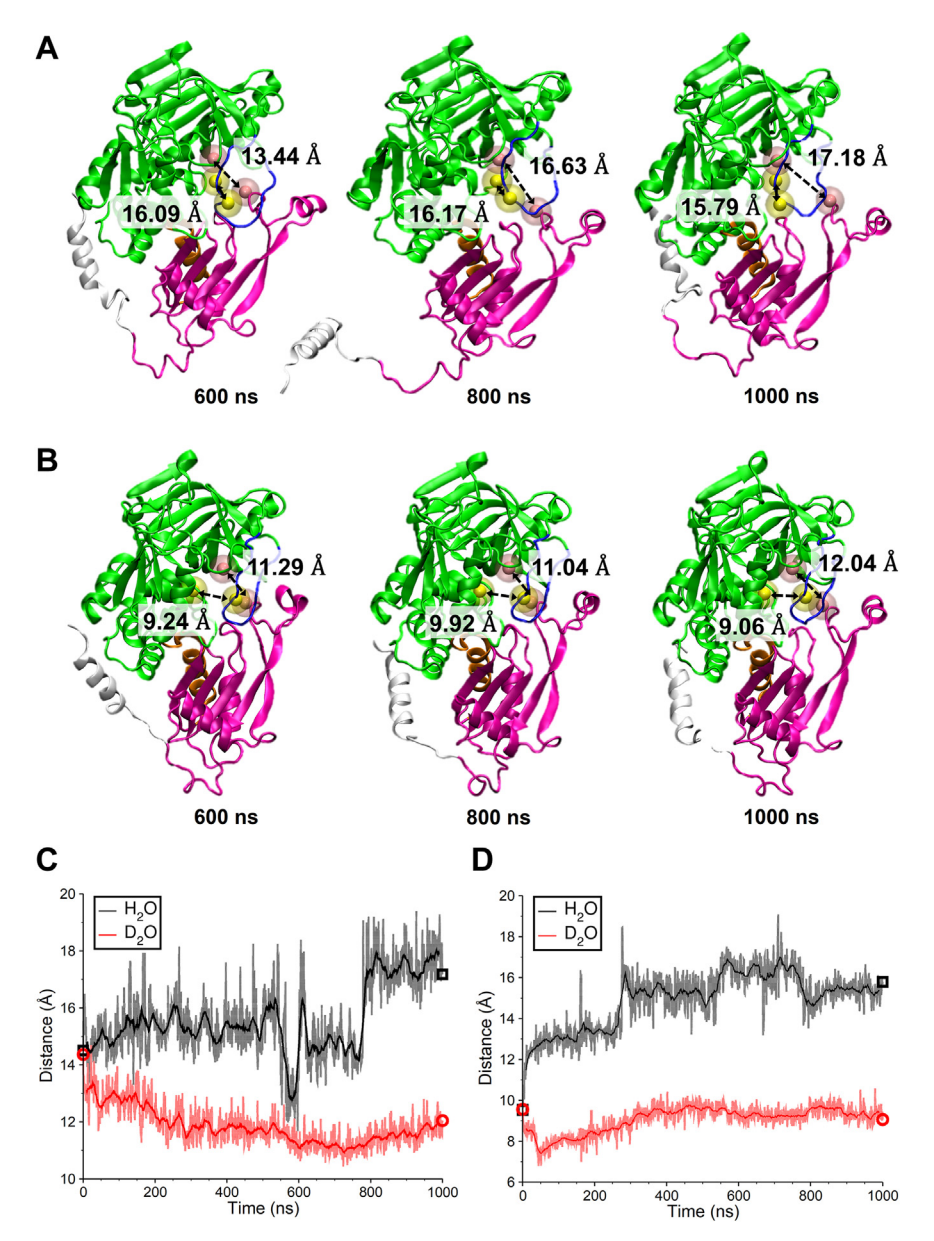


Figure 7. Evolution of PhdA structure during MD simulations. Representative snapshots at 600 ns, 800 ns and 1000 ns for PhdA in (A) H₂O and (B) D₂O. The domains are color-coded as follows: N-terminal prFMN binding domain (green), central α-helix (gray), oligomerization domain (green), C-terminal α-helix (gray), active site loop (gray). The COMs of R159 and I416 are presented in gray1 pink whereas COMs of prFMN and E269 in gray2 in gray3 per each snapshot, the respective COM distances are shown. Temporal evolution of COM distances for (gray2) prFMN–E269.

Our simulations suggest that D_2O leads to significant structural changes in the active site which can affect catalysis.

D_2O promotes intra-protein hydrogen bonds resulting in a more compact structure

To ascertain why these solvent-specific differences exist in the protein conformations, the protein-solvent and intraprotein hydrogen bonds were calculated over the last 500 ns of the trajectories. In D_2O the protein exhibited fewer protein-solvent hydrogen bonds (Fig. 8A) and more intra-protein hydrogen bonds (Fig. 8B). Additionally, the hydrogen bond autocorrelation functions were calculated to analyze their lifetimes in both simulations (data summarized in Table S1).

Interestingly, it was found that the probability of persistence of hydrogen bonds decayed slower in D₂O for both protein-solvent and intra-protein hydrogen bonding. The intra-protein hydrogen bonds were also generally found to persist significantly longer than hydrogen bonds with the solvent. These observations agree with the work of Sheu *et al.*, who performed MD simulations on test polypeptides (alpha helix with 13-mer: CH₃OC-SDELAKLLRLHAG-NH2, beta-hairpin 12-mer: CH₃OC-V5PGV5-NH2) in H₂O and D₂O and found that D₂O did not facilitate as significant a decrease in the activation energy for hydrogen bonding as H₂O resulting in a decreased decay rate (45). Additional analyses regarding the hydrogen bonding behavior in both simulations are presented in the Supporting Information.

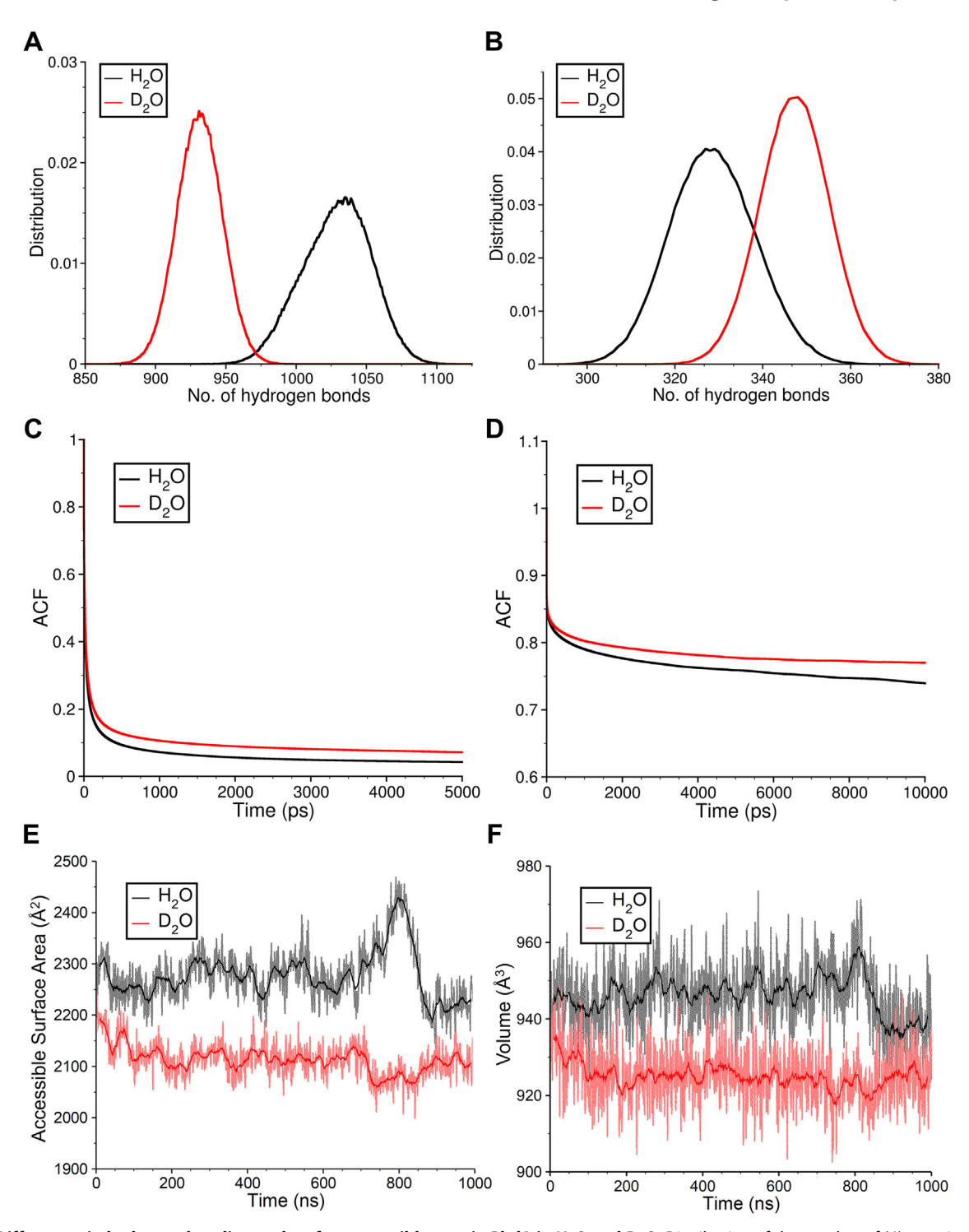


Figure 8. Differences in hydrogen bonding and surface accessible area in PhdA in H₂O and D₂O. Distribution of the number of (A) protein-solvent and (B) intra-protein hydrogen bonds. Autocorrelation functions (ACF) for (C) protein-solvent, and (D) intra-protein hydrogen bonding. Analyses in (A-D) were performed for the final 500 ns of the simulation trajectory. Evolution of protein (E) solvent accessible surface area (SASA), and (F) volume, throughout the simulation. For (E and F) translucent background lines display data points from the entire simulation trajectory (1,000,000 points) while the solid foreground lines display smoother running averages considering every 2000 points.

Previous studies suggest that proteins compress in D₂O, leading to a more compact shape (35, 45). To validate this behavior, the solvent-accessible surface area (SASA) and volume of the protein were also calculated for the simulations. It was observed that the D₂O-solvated protein showed lower values of SASA (Fig. 8E) and volume (Fig. 8F) throughout the

time course, indicating that D2O induced a more compact protein conformation. Furthermore, upon examining the unique intra-protein hydrogen bonds observed for the final 20 ns of the simulation, (Table S2), we observed that D2O promotes more hydrogen bonds in regions along the active site, including the active site loop. Overall, this analysis shows

$$E \xrightarrow{*k_{1}.S} E.S \xrightarrow{*k_{3}} E.I_{1} \xrightarrow{*k_{5}} E.I_{2} \xrightarrow{k_{77.7.7}} E_{D.I_{2}} \xrightarrow{k_{7D}} E_{D.I_{3}} \xrightarrow{k_{9}} E.P_{D} \xrightarrow{k_{10}} E.P_{D}$$

Figure 9. Proposed kinetic mechanism for PhdA consistent with the observed solvent isotope effects. Various enzyme forms are as labeled in Figure 1. k_7 and k_{7D} are the rate constants for proton transfer involving H and D respectively. χ is the solvent D-atom fraction and L is the total concentration of all H and D. The *inverse* medium effect is a "general" effect and is depicted by (*) on steps k_1 through k_5 .

that the lower R-I distances and a more compact active site observed in D2O can be rationalized through the differences in protein-solvent and intra-protein hydrogen bonding between the two solvents.

Discussion

The prFMN-dependent family of decarboxylases, collectively known as UbiD-like enzymes, are now known to be widely distributed in microbes. We previously showed that the recently discovered UbiD-like enzyme, phenazine-1carboxylate decarboxylase, (PhdA) could decarboxylate a range of polyaromatic carboxylic acids. Here we have focused on defining the kinetics and mechanism of the enzyme by using the slow substrate DQCA to probe the nature of the rate-determining step. The unusual, inverse solvent isotope effect associated with the decarboxylation of DOCA prompted us to undertake a more detailed investigation of the effect of solvent on the rate of reaction and the stability of the enzyme. The experimental observations are consistent with, and to some extent rationalized by, our MD simulations of the response of the protein structure to D_2O .

Recent studies on UbiD-like enzymes have suggested the importance of domain motions in catalysis. For example, stopped-flow spectroscopy indicates that the dimeric UbiDlike enzyme FDC exhibits negative cooperativity between the two subunits arising from a conformational change that facilitates inter-conversion between the "fast, tight" and the "slow, loose" active sites (46). Studies on vanillic acid decarboxylase suggest that "open" and "closed" conformers of the enzyme have different affinities for reaction intermediates that may be important for catalysis (44). Our studies suggest that similar domain motions are important in the mechanism of PhdA and that these may, in part, account for the unusual kinetic behavior observed in D2O, which is accentuated by using the slow substrate DOCA.

MD simulations on PhdA in H₂O and D₂O suggest that D₂O increases intra-protein H-bonding, which is consistent with the slight increase in ΔG_{unfold} observed in D_2O . The simulations also indicate that D2O affords a more compact structure to the protein, including stabilizing the active site loop as well as promoting domain closure towards a more "closed"-like conformer. These features would be expected to stabilize the Michaelis complex and subsequent reaction intermediates. The lower K_M values observed for both substrates in D₂O and the significantly tighter K_I^{app} measured for DQCA in D₂O are consistent with the MD simulations. Moreover, the D2O-

induced conformational shift towards the catalytically active form of the enzyme rationalizes the inverse D2OV/K effect.

The apparently contradictory solvent isotope effects exhibited by PhdA in the decarboxylation of DQCA, and to a lesser extent PCA, are mechanistically informative. A key point is that the two SIE values are measured by different methods: PIE is measured by internal competition, whereas $^{D2O}V/K$ is measured by comparing reaction rates. We propose the kinetic mechanism shown in Figure 9 that best explains the SIE data (refer to Supporting information for derivation).

We assume that step k_7 , which involves proton transfer to the product, is subject to a *normal* isotope effect (k_{7D}). We also assume that CO₂ release is functionally irreversible, effectively dividing the reaction into two halves. D2OV/K, which is best considered as a medium effect arising from D2O-induced changes to the enzyme structure, is manifested in steps k_1 through k_5 which encompasses the rate-determining step. On the other hand, PIE incorporates the proton transfer step, k_{7} and arises in the second half of the reaction. Thus, the two isotope effects occur in separate regions of the kinetic mechanism and are independent of each other. Decarboxylation, being an irreversible step, will prevent the E.I₂ complex from partitioning back, and thus, the latter half of the reaction would be insensitive to any prior H/D exchange on Glu269 (refer to SI, Mechanism 2) (25). Therefore, for the isotope effect on k_7 to be expressed in PIE, H/D exchange of Glu269 with the solvent (E.I₂ to E_H.I₂/E_D.I₂) must occur after decarboxylation and be rapid with respect to proton transfer $(k_{h2} >> k_7)$.

The proton inventory of V_{max} , provides further support for the proposed mechanism. As shown in Figure 4B, the rate initially increases with increasing solvent D-atom fraction. But at high D-atom fractions, the reaction rate slows down as the normal isotope effect on proton transfer becomes increasingly rate limiting, thereby offsetting the inverse medium isotope effect associated with the earlier steps.

In conclusion, the kinetics of PhdA decarboxylation suggest that protein conformational changes play a kinetically significant role under both V_{max}/K_M and V_{max} conditions. Even for the slow substrate DQCA, under V_{max} conditions, the proton inventory analysis indicates that proton transfer is only \sim 10% rate limiting. Conformational switching between "open" and "closed" forms appears to be a general feature of UbiD-like enzymes, although whether such motions are kinetically significant in the decarboxylation reactions catalyzed by other members of this enzyme family remains to be determined. We note that there is growing interest in using UbiD-like decarboxylases for biocatalytic applications. In this context, our results suggest that

engineering these enzymes (or optimizing solvent systems) to increase the stability of the "closed" form may have the added benefit of improving their catalytic efficiency.

Experimental procedures

Reagents and chemicals

Phenazine-1-carboxylic acid (PCA, 98% pure), phenazine (98% pure), 2,3-dimethylquinoxaline-5-carboxylic acid (DQCA, 95% pure) and 2,3-dimethylquinoxaline (DQ, 97% pure) were purchased from Apollo Scientific Co, Sigma Aldrich Co, 1 ClickChemistry Inc or Thermo Fisher Scientific Co and used without further purification. Deuterium oxide (99.8% atom D) was purchased from Thermo Fisher Co. All other reagents were purchased from Sigma Aldrich Co or Thermo Fisher Co.

Purification and Reconstitution of PhdA

E. coli BL21DE3 cells (Invitrogen) were co-transformed with pET20b(+) containing phdA and pET28b(+) containing ubiX from P. aeruginosa (paubiX). Cells were cultivated at 37°C in LB broth with 50 µg/ml each of Ampicillin and Kanamycin. After an OD₆₀₀ of 0.6 to 0.8, the cultures were supplemented with 0.1 mM IPTG and 1 ml prenol. Cells were incubated overnight (20 °C, 170 rpm), harvested and the PhdA was purified through Ni-affinity chromatography (21). Purified PhdA was reconstituted in vitro with prFMN, quantified via Bradford Assay, and tested for PCA decarboxylation under standard conditions as described (21). The activity did not vary significantly between different batches of the reconstituted enzyme.

HPLC and LC-MS analysis

The decarboxylation of substrates was monitored using the discontinuous HPLC-based assay previously described (21). The incorporation of solvent deuterium into the product was monitored by LC-MS as previously described (21).

pL - rate profiles

The following buffers were used at 0.1 M concentrations: sodium citrate (pL 5.5-6), Bis-Tris-Cl (pL 6-6.5), potassium phosphate (pL 6.5-8) and Tris-Cl (pL 8-8.5). Buffers were prepared in H₂O/D₂O and titrated with HCl/DCl or NaOH/ NaOD to the desired pH. For phosphate buffers, KH2PO4 and K₂HPO₄ stocks were prepared in H₂O/D₂O and titrated. For D_2O buffers, the atom fraction of $D(\chi)$ was re-calculated based on protium added from the buffer components (in most cases $\chi > 0.99$). Corrections were applied to the pH-meter readings using the equation (14):

$$pD = pH_{meter} + 0.076\chi^2 + 0.3314 \chi + 0.00009$$

Activity assays were performed at room temperature (20-22 °C) and consisted of 0.1 M buffer, 0.1 to 0.5 μM reconstituted PhdA and different concentrations of substrates. For PCA, 10 to 15 µM substrate was added under V_{max}/K_M conditions whereas for V_{max} , 500 to 1000 μM PCA was used. Similarly, for DQCA, 30 to 50 μM of the acid was used for V_{max}/K_M and 5 to 10 mM for V_{max} . Reactions were quenched by adding 500 mM NaOH (final concentration) and analyzed by HPLC. Reaction rates, normalized by enzyme concentration (ν/E_t) , were plotted as a function of pL and fit to the following equation (23):

$$v / E_t = \frac{(v/E_t)_{max}}{1 + 10^{pK_{a1} - pL} + 10^{pL - pK_{a2}}}$$

Where it is assumed that the pL-rate behavior of PhdA arises from the titration of 2 ionizable groups, each with a single pK_a. $(v/E_t)_{max}$ is the pL-independent rate, pK_{a1} corresponds to the group that needs to be deprotonated for activity and pKa2 is for the residue that needs to be protonated.

Solvent isotope effects

Potassium phosphate buffers (pH or pD = 7) in H_2O and D₂O were made as described above and added volumetrically to obtain mixed isotopic buffers. The atom fraction of D (x) was adjusted by applying the necessary corrections (23). All subsequent reactions were performed in these buffers.

For measuring PIE, reactions containing PhdA (0.2 µM) and PCA (15 µM) were performed in mixed isotopic buffers and quenched after 20 s. Alternatively, 1 µM PhdA was reacted with 50 µM DQCA and quenched after 15 min. Samples were analyzed by LC-MS in positive ion mode. Due to the substantial presence (\sim 10%) of naturally occurring ¹³C-isotopes that also incorporate D, the LC-MS peaks for [M + H], [M + H + 1 and [M + H + 2] changed with χ . Thus, the fractional incorporation of deuterium into the products $(\chi_{D,product})$ was determined as:

$$\chi_{D,product} \ = \frac{[M\!+\!H\!+\!1]\!+\![M\!+\!H\!+\!2]}{[M\!+\!H]\!+\![M\!+\!H\!+\!1]\!+\![M\!+\!H\!+\!2]}$$

The values of $\chi_{D,product}$ thus obtained were plotted against χ and fit to Equation 1 described in the main text.

Proton inventories were obtained under either V_{max} (5–10 mM DQCA) or V_{max}/K_M (50–100 μ M DQCA) conditions. The ratio of the rate in mixed isotopic water to $H_2O(v_x/v_y)$ v_0) was plotted as a function of the D-atom fraction, χ and fitted to Equations 2–5 (see Results section) as applicable (28).

For midpoint SIE (24), the rate of DQCA decarboxylation (v) was monitored at low substrate concentrations (V_{max}/K_M conditions) in H_2O (χ = 0), D_2O (χ = 0.99) and χ = 0.5, following which $v_{0.5}/v_0$ and $v_{0.99}/v_0$ were calculated. Later, Equations 2–4 were solved for $\chi = 0.99$ to determine the parameters ϕ_T , Z, and ϕ_R . The experimental value of $v_{0.5}/v_0$ was then compared to the theoretical values calculated for the different mechanisms represented by Equations 2-4 at $\chi = 0.5$.

Protein unfolding

All reactions were performed at 20°C. Stocks of 9 M urea in H₂O or D₂O were added to 0.1 µM PhdA in 0.1 M potassium phosphate buffer (pL = 7) to achieve different concentrations of urea. The samples were incubated for 60 to 90 min after which protein fluorescence emission spectra were recorded. Excitation wavelength = 295 nm; emission spectrum recorded between 310 to 470 nm. The average



wavelength of emission (λ_{avg}) at each concentration of urea was calculated by (47):

$$\lambda_{avg} = \sum_{i=1}^{N} (I_i \lambda_i) / \sum_{i=1}^{N} I_i$$

Where N is the total number of data points and λ_i , I_i are the wavelength and intensity of the i^{th} data point. The normalized λ_{avg} values were plotted against urea concentration and fitted to the following equation (48):

$$f_U = \frac{F + U \cdot e^{-m(K_{1/2} - x)}}{1 + e^{-m(K_{1/2} - x)}}$$

Here, f_U is the unfolded fraction as a function of urea concentration (x), F, U are values of f_U for the folded and unfolded protein respectively, $K_{1/2}$ is the value of x for f_U = 0.5 and m describes the change in $K_{1/2}$ as a function of x. The free energy of unfolding was calculated as ΔG_U = m.R.T. $K_{1/2}$ (48). Here, R is the gas constant and T = 293.15 K.

Inhibition studies

Reactions were setup in potassium phosphate buffer (pH or pD = 7) and consisted of 0.2 μ M PhdA, 50 μ M PCA and varying concentrations of DQCA. The residual normalized rate (v/E_t) was plotted against DQCA concentration and fit to the following equation, assuming competitive inhibition (49):

$$v / E_t = \frac{k_{cat} \cdot S}{S + \left(1 + \frac{I}{K_I}\right) K_M}$$

Here, I is the independent variable (DQCA concentration), $S = 50 \mu M$ is the concentration of PCA, k_{cat} and K_M are the steady-state parameters for PCA and K_I is the apparent inhibition constant for DQCA.

Data fitting and mathematical modeling

All data were fitted using Origin 2022 graphing software. Steady-state kinetic expressions were derived using Wolfram Mathematica v13.2. Please refer to SI for a detailed explanation and derivation of all models considered.

Molecular dynamics simulations

Molecular Dynamics (MD) simulations were performed using the GROMACS package (50). The crystal structure of PhdA monomer (PDB:7PDA) (22) was solvated in a 100 Å x 100 Å x 100 Å cubic box with \sim 30,000 solvent (H₂O or D₂O) molecules. The protein was parameterized using the CHARMM36 force field (51), whereas the cofactor was parameterized using the CHARMM general force field (52). The TIP3P water model was used to represent H₂O (53), whereas D₂O was parameterized using the TIP3P-HW model (54). Additionally, 150 mM KCl ions were used for creating proper physiological conditions, and extra neutralizing ions were added to maintain an overall charge-neutral system. With a 12 Å cutoff, the Particle-Mesh Ewald (PME) approach was utilized for long-range electrostatics (55). Similarly, the van der Waals cutoff was also set to

12 Å. Initially, the model systems were energy minimized using the steepest descent minimization algorithm (56). The MD simulations were performed at a temperature of 298 K, with periodic boundaries, using the NPT thermodynamic ensemble, where temperature and pressure control was achieved using Nose-Hoover thermostat and Parrinello-Rahman barostat (57-59). The trajectory was recorded every 1 ps, giving a total of 1,000,000 frames for each of the 1 µs simulations. The entire trajectory was analyzed for the root mean squared deviation (RMSD), free energy landscape (FEL), and the evolution of R159-I416 and prFMN-E269 distances. Allowing the system to equilibrate during the initial 500 ns, the trajectories from 500 to 1000 ns were used to analyze the root mean squared fluctuation (RMSF) as well as protein-solvent and intraprotein hydrogen bonding using GROMACS in-built packages and Visual Molecular Dynamics (60).

Data availability

All data presented are contained within the manuscript or the supporting information.

Supporting information—Describing solvent viscosity studies, computational data, derivation of kinetic models, equations, and other supporting figures referred to in the main text; a table of all unique intra-protein H bonds for the H_2O and D_2O solvated proteins that were observed in the simulations (14, 24, 28–31, 36, 61–65).

Acknowledgments—We thank Prof. Diane Newman (Caltech) for kindly providing us with the expression strain for PhdA. We also thank Prof. Bruce Palfey (University of Michigan) and Ross Stein, PhD (Loxo Oncology) for their valuable insights on solvent isotope effects.

Author contributions—P. M. D. and S. Y. J. investigation; P. M. D., S. Y. J., S. A. D., and E. N. G. M. writing—original draft; P. M. D., S. Y. J., S. A. D., and E. N. G. M. writing—review and editing; P. M. D., S. Y. J., S. A. D., and E. N. G. M. methodology; P. M. D., S. Y. J. and S. A. D. formal analysis; P. M. D. and E. N. G. M. conceptualization; S. A. D. and E. N. G. M. funding acquisition; E. N. G. M. supervision; E. N. G. M. project administration.

Funding and additional information—This work was funded by grants CHE 2203729 and CHE 1904759 from the National Science Foundation to E. N. G. M. S. A. D. and S. Y. J. acknowledge the Advanced Research Computing Facility at Virginia Tech, and funding from GlycoMIP, a National Science Foundation Materials Innovation Platform (DMR-1933525). S. Y. J. thanks Dr Lakshmi Kumar Kunche for their guidance in using several GROMACS functionalities in analyzing MD simulations.

Conflict of interest—The authors declare that they have no conflicts of interest with the contents of this article.

Abbreviations—The abbreviations used are: DQCA, 2,3-dimethylquinoxaline-5-carboxylic acid; PCA, phenazine-1-carboxylic acid; PhdA, phenazine-1-carboxylic acid decarboxylase; prFMN, prenylated-flavin mononucleotide.



References

- 1. White, M. D., Payne, K. A., Fisher, K., Marshall, S. A., Parker, D., Rattray, N. J., et al. (2015) UbiX is a flavin prenyltransferase required for bacterial ubiquinone biosynthesis. Nature 522, 502-506
- 2. Payne, K. A. P., White, M. D., Fisher, K., Khara, B., Bailey, S. S., Parker, D., et al. (2015) New cofactor supports α , β -unsaturated acid decarboxylation via 1,3-dipolar cycloaddition. Nature 522, 497-501
- 3. Meganathan, R. (2001) Ubiquinone biosynthesis in microorganisms. FEMS Microbiol. Lett. 203, 131-139
- 4. Aleku, G. A., Saaret, A., Bradshaw-Allen, R. T., Derrington, S. R., Titchiner, G. R., Gostimskaya, I., et al. (2020) Enzymatic C-H activation of aromatic compounds through CO2 fixation. Nat. Chem. Biol. 16,
- 5. Kawanabe, K., Aono, R., and Kino, K. (2021) 2,5-Furandicarboxylic acid production from furfural by sequential biocatalytic reactions. J. Biosci. Bioeng. 132, 18-24
- 6. Payer, S. E., Faber, K., and Glueck, S. M. (2019) Non-oxidative enzymatic (de)carboxylation of (hetero)aromatics and acrylic acid derivatives. Adv. Syn. Catal. 361, 2402-2420
- 7. Leys, D. (2018) Flavin metamorphosis: cofactor transformation through prenylation. Curr. Opin. Chem. Biol. 47, 117-125
- 8. Piano, V., Palfey, B. A., and Mattevi, A. (2017) Flavins as covalent catalysts: new mechanisms emerge. Trends Biochem.Sci. 42, 457-469
- 9. Leys, D., and Scrutton, N. S. (2016) Sweating the assets of flavin cofactors: new insight of chemical versatility from knowledge of structure and mechanism. Curr. Opin. Struct. Biol. 41, 19-26
- 10. Kaneshiro, A. K., Koebke, K. J., Zhao, C., Ferguson, K. L., Ballou, D. P., Palfey, B. A., et al. (2021) Kinetic analysis of transient intermediates in the mechanism of prenyl-flavin-dependent ferulic acid decarboxylase. Biochemistry **60**, 125–134
- 11. Bailey, S. S., Payne, K. A. P., Saaret, A., Marshall, S. A., Gostimskaya, I., Kosov, I., et al. (2019) Enzymatic control of cycloadduct conformation ensures reversible 1,3-dipolar cycloaddition in a prFMN-dependent decarboxylase. Nat. Chem. 11, 1049-1057
- 12. Bailey, S. S., Payne, K. A. P., Fisher, K., Marshall, S. A., Cliff, M. J., Spiess, R., et al. (2018) The role of conserved residues in Fdc decarboxylase in prenylated flavin mononucleotide oxidative maturation, cofactor isomerization, and catalysis. J. Biol. Chem. 293, 2272-2287
- 13. Ferguson, K. L., Eschweiler, J. D., Ruotolo, B. T., and Marsh, E. N. G. (2017) Evidence for a 1,3-dipolar cyclo-addition mechanism in the decarboxylation of phenylacrylic acids catalyzed by ferulic acid decarboxylase. J. Am. Chem. Soc. 139, 10972-10975
- 14. Ferguson, K. L., Arunrattanamook, N., and Marsh, E. N. G. (2016) Mechanism of the novel prenylated flavin-containing enzyme ferulic acid decarboxylase probed by isotope effects and linear free-energy relationships. *Biochemistry* **55**, 2857–2863
- 15. Lin, F., Ferguson, K. L., Boyer, D. R., Lin, X. N., and Marsh, E. N. G. (2015) Isofunctional enzymes PAD1 and UbiX catalyze formation of a novel cofactor required by ferulic acid decarboxylase and 4-hydroxy-3-polyprenylbenzoic acid decarboxylase. ACS Chem. Biol. 10, 1137-1144
- 16. Payer, S. E., Marshall, S. A., Bärland, N., Sheng, X., Reiter, T., Dordic, A., et al. (2017) Regioselective para-carboxylation of catechols with a prenylated flavin dependent decarboxylase. Angew. Chem. 56, 13893-13897
- 17. Costa, K. C., Moskatel, L. S., Meirelles, L. A., and Newman, D. K. (2018) PhdA catalyzes the first step of phenazine-1-carboxylic acid degradation in Mycobacterium fortuitum. J. Bacteriol. 200, e00763-17
- 18. Price-Whelan, A., Dietrich, L. E. P., and Newman, D. K. (2006) Rethinking 'secondary' metabolism: physiological roles for phenazine antibiotics. Nat. Chem. Biol. 2, 71-78
- 19. Gellatly, S. L., and Hancock, R. E. W. (2013) Pseudomonas aeruginosa: new insights into pathogenesis and host defenses. Pathog. Dis. 67,
- 20. Mavrodi, D. V., Parejko, J. A., Mavrodi, O. V., Kwak, Y. S., Weller, D. M., Blankenfeldt, W., et al. (2013) Recent insights into the diversity, frequency and ecological roles of phenazines in fluorescent Pseudomonas spp. Environ. Microbiol. 15, 675-686

- 21. Datar, P. M., and Marsh, E. N. G. (2021) Decarboxylation of aromatic carboxylic acids by the prenylated-FMN-dependent enzyme phenazine-1carboxylic acid decarboxylase. ACS Catal. 11, 11723–11732
- 22. Gahloth, D., and Leys, D. (2021) Crystal Structure of Phenazine 1-carboxylic Acid Decarboxylase from Mycobacterium Fortuitum, Protein Data Base entry 7PDA. https://doi.org/10.2210/pdb2217PDA/pdb
- 23. Quinn, D. M., and Sutton, L. D. (1991). In: Cook, P. F., ed. Theoretical Basis and Mechanistic Utility of Solvent Isotope Effects in Enzyme Mechanism from Isotope effects, CRC Press, Boca Raton, FL, USA: 73-126
- 24. Schowen, K. B., and Schowen, R. L. (1982) Solvent isotope effects of enzyme systems. Methods Enzymol. 87, 551-606
- 25. Northrop, D. B. (1981) Limits on the expression of enzyme-mediated solvent isotope effects. J. Am. Chem. Soc. 103, 1208-1212
- 26. Robbins, J. M., and Ellis, H. R. (2012) Identification of critical steps governing the two-component alkanesulfonate monooxygenase catalytic mechanism. Biochemistry 51, 6378-6387
- 27. Karsten, W. E., Lai, C.-J., and Cook, P. F. (1995) Inverse solvent isotope effects in the NAD-malic enzyme reaction are the result of the viscosity difference between D2O and H2O: implications for solvent isotope effect studies. J. Am. Chem. Soc. 117, 5914-5918
- 28. Venkatasubban, K. S., and Schowen, R. L. (1984) The proton inventory technique. Crit. Rev. Biochem. 17, 1-44
- 29. Schowen, R. L. (1978). In: Gandour, R. D., Schowen, R. L., eds. Catalytic Power and Transititon State Stabilization in Transition States of Biochemical Processes, Springer, New York: 77-114
- 30. Stein, R. L. (1981) Analysis of kinetic isotope effects on complex reactions utilizing the concept of the virtual transition state. J. Org. Chem. 46,
- 31. Quinn, D. M. (1987) Acetylcholinesterase: enzyme structure, reaction dynamics, and virtual transition states. Chem. Rev. 87, 955-979
- 32. Maybury, R. H., and Katz, J. J. (1956) Protein denaturation in heavy water. Nature 177, 629-630
- 33. Hermans, J. J., and Sheraga, H. A. (1959) The thermally induced configurational change of ribonuclease in H2O and D2O. Biochim. Biophys. Acta 36, 534-535
- 34. Parker, M. J., and Clarke, A. R. (1997) Amide backbone and water-related H/D isotope effects on the dynamics of a protein folding reaction. Biochemistry 36, 5786-5794
- 35. Cioni, P., and Strambini, G. B. (2002) Effect of heavy water on protein flexibility. *Biophys. J.* **82**, 3246–3253
- 36. Northrop, D. B. (1981) The expression of isotope effects on enzymecatalyzed reactions. Annu. Rev. Biochem. 50, 103-131
- 37. Northrop, D. (1998) On the meaning of K_m and V/K in enzyme kinetics. J. Chem. Educ. 75, 1153-1157
- 38. Roberts, G. W., and Leys, D. (2022) Structural insights into UbiD reversible decarboxylation. Curr. Opin. Struct. Biol. 75, 102432
- 39. Papaioannou, A., Kuyucak, S., and Kuncic, Z. (2015) Molecular dynamics simulations of Insulin: elucidating the conformational changes that enable its binding. PLoS One 10, e0144058
- 40. Guterres, H., and Im, W. (2020) Improving protein-ligand docking results with high-throughput molecular dynamics simulations. J. Chem. Inf. Model. **60**, 2189–2198
- 41. Martínez, L. (2015) Automatic identification of mobile and rigid substructures in molecular dynamics simulations and fractional structural fluctuation analysis. PLoS One 10, e0119264
- 42. Maisuradze, G. G., and Leitner, D. M. (2007) Free energy landscape of a biomolecule in dihedral principal component space: Sampling convergence and correspondence between structures and minima. Proteins: Struct. Funct. Bioinf. 67, 569-578
- 43. Daura, X., Gademann, K., Jaun, B., Seebach, D., van Gunsteren, W. F., and Mark, A. E. (1999) Peptide folding: when simulation meets experiment. Angew. Chem. 38, 236-240
- 44. Marshall, S. A., Payne, K. A. P., Fisher, K., Titchiner, G. R., Levy, C., Hay, S., et al. (2021) UbiD domain dynamics underpins aromatic decarboxylation. Nat. Comm. 12, 5065
- 45. Sheu, S.-Y., Schlag, E. W., Selzle, H. L., and Yang, D.-Y. (2008) Molecular dynamics of hydrogen bonds in protein-D2O: the solvent isotope effect. J. Phys. Chem. A. 112, 797–802



- 46. Kaneshiro, A. K., Datar, P. M., and Marsh, E. N. G. (2023) Negative cooperativity in the mechanism of prenylated-flavin-dependent ferulic acid decarboxylase: a proposal for a "two-stroke" decarboxylation cycle. *Biochemistry* 62, 53–61
- 47. Royer, C. A., Mann, C. J., and Matthews, C. R. (1993) Resolution of the fluorescence equilibrium unfolding profile of trp aporepressor using single tryptophan mutants. *Protein Sci.* 2, 1844–1852
- Parisi, M., Mazzini, A., Robert, T. S., Ramoni, R., Grolli, S., and Favilla, R. (2003) Unfolding and refolding of porcine odorant binding protein in guanidinium hydrochloride: equilibrium studies at neutral pH. *Biochim. Biophys. Acta Proteins Proteomics* 1652, 115–125
- **49.** Fersht, A. (1977) *Enzyme Structure and Mechanism*, W.H. Freeman and Company, New York, NY
- Abraham, M. J., Murtola, T., Schulz, R., Páll, S., Smith, J. C., Hess, B., et al. (2015) GROMACS: high performance molecular simulations through multi-level parallelism from laptops to supercomputers. SoftwareX 1-2, 19–25
- Huang, J., and MacKerell, A. D., Jr. (2013) CHARMM36 all-atom additive protein force field: validation based on comparison to NMR data. J. Comput. Chem. 34, 2135–2145
- 52. Vanommeslaeghe, K., Hatcher, E., Acharya, C., Kundu, S., Zhong, S., Shim, J., et al. (2010) CHARMM general force field: a force field for drug-like molecules compatible with the CHARMM all-atom additive biological force fields. J. Comput. Chem. 31, 671–690
- Mark, P., and Nilsson, L. (2001) Structure and dynamics of the TIP3P, SPC, and SPC/E water models at 298 K. J. Phys. Chem. A. 105, 9954–9960
- Linse, J.-B., and Hub, J. S. (2021) Three- and four-site models for heavy water: SPC/E-HW, TIP3P-HW, and TIP4P/2005-HW. J. Chem. Phys. 154, 194501

- Darden, T., York, D., and Pedersen, L. (1993) Particle mesh Ewald: an N·log(N) method for Ewald sums in large systems. J. Chem. Phys. 98, 10089–10092
- Curry, H. B. (1944) The method of steepest descent for non-linear minimization problems. Q. Appl. Math. 2, 258–261
- 57. Nosé, S. (1984) A molecular dynamics method for simulations in the canonical ensemble. *Mol. Phys.* 52, 255–268
- Hoover, W. G. (1985) Canonical dynamics: equilibrium phase-space distributions. *Phys. Rev. A.* 31, 1695–1697
- Parrinello, M., and Rahman, A. (1981) Polymorphic transitions in single crystals: a new molecular dynamics method. J. Appl. Phys. 52, 7182–7190
- Humphrey, W., Dalke, A., and Schulten, K. (1996) VMD: visual molecular dynamics. J. Mol. Graph. 14, 27–38
- Haynes, W. M. (2014) CRC Handbook of Chemistry and Physics, CRC press, Boca Raton
- **62.** Gadda, G., and Sobrado, P. (2018) Kinetic solvent viscosity effects as probes for studying the mechanisms of enzyme action. *Biochemistry* **57**, 3445–3453
- 63. Stein, R. L. (1985) Transition-state properties for the association of α-1-protease inhibitor with porcine pancreatic elastase. J. Am. Chem. Soc. 107, 6039–6042.
- 64. Cleland, W. W. (1975) Partition analysis and the concept of net rate constants as tools in enzyme kinetics. *Biochemistry* 14, 3220–3224
- 65. Róg, T., Murzyn, K., Milhaud, J., Karttunen, M., and Pasenkiewicz-Gierula, M. (2009) Water isotope effect on the phosphatidylcholine bilayer properties: a molecular dynamics simulation study. *J. Phys. Chem. B* 113, 2378–2387

